Phase segregation and miscibility of TiO_x nanocomposites in Gd-doped ceria solid electrolyte material

Authors

Junying Li[a], Prahlad K. Routh[a]*, Yuanyuan Li[a], Anna Plonka[a], Evgeniy Makagon[b], Igor Lubomirsky[b]* and Anatoly Frenkel[ac]*

[a]Department of Materials Science and Chemical Engineering, Stony Brook University, Stony Brook, New York, 11794, United States

[b]Department of Molecular Chemistry and Materials Science, Weizmann Institute of Science, Rehovot, 761001, Israel

[c]Chemistry Division, Brookhaven National Laboratory, Upton, New York, 11973, USA

Correspondence email: prahladkumar.routh@stonybrook.edu; igor.lubomirsky@weizmann.ac.il; anatoly.frenkel@stonybrook.edu

Funding information National Science Foundation (grant No. DMR-1911592 to Anatoly Frenkel, Junying Li, Yuanyuan Li, Prahlad K. Routh); Binational Science Foundation (Israel) (grant No. 2018717 to Igor Lubomirsky).

Synopsis Local structure of titania-ceria composites in a Gd-doped ceria solid electrolyte material is obtained by a combination of X-ray absorption fine structure and X-ray diffraction at the entire range of Ti composition. We discovered a compositional region (between 19 and 57%) with strongly distorted TiO_6 units and coexisting of Ce(III) and Ce(IV), i.e., optimized for oxygen transport conduction and in agreement with the enhanced electro-chemo-mechanical effect previously observed in this composition range.

Abstract Electro-chemo-mechanical (ECM) coupling refers to the mechanical deformation due to electrochemically driven compositional change in a solid. An ECM actuator producing micron-size displacements and long-term stability at room temperature was reported recently, which comprised of a 20 mol% Gd-doped ceria (20GDC), a solid electrolyte membrane, placed between two working bodies made of TiO_x/20GDC (Ti-GDC) nanocomposites with Ti concentration of 38 mol%. The volumetric changes originating from the oxidation or reduction in the local TiO_x units are hypothesized to be the origin of mechanical deformation in the ECM actuator. Studying the Ti concentration-dependent structural changes

in the Ti-GDC nanocomposites is therefore needed for 1) understanding the mechanism of dimensional changes in the ECM actuator and 2) maximizing the ECM response. We report the systematic investigation of the local structure of the Ti and Ce ions in the Ti-GDC in a broad range of Ti concentrations by using synchrotron X-ray absorption spectroscopy (XAS) and X-ray diffraction. Our main finding is that, depending on the Ti concentration, Ti atoms either form a cerium titanate or segregate into TiO_2 anatase-like phase. The transition region between these two regimes with Ti(IV) concentration between 19 and 57% contained strongly disordered TiO_x units dispersed in 20GDC containing Ce(III) and Ce(IV) and hence rich with oxygen vacancies. As a result, this transition region is proposed to be the most advantageous for developing ECM-active materials.

Keywords: X-ray absorption spectroscopy, electro-chemo-mechanical effect, local structural distortions

1. Introduction

Electro-chemo-mechanical (ECM) coupling (Bishop *et al.*, 2014, Bishop *et al.*, 2017, Swallow *et al.*, 2014, Tuller & Bishop, 2011) generates large strain and dimensional changes in nanocomposites induced by the electrochemically driven compositional changes in the solid. Although the strain induced by the ECM effect is detrimental to Li-ion batteries (Sethuraman *et al.*, 2010, Swallow *et al.*, 2014, Wang *et al.*, 2015), the macroscopic strain resulting from the compositional changes across the device is attractive for an actuation mechanism. Swallow et al. (Swallow *et al.*, 2017) demonstrated the first high-temperature (550 °C), low-voltage ECM actuator. The induced strain was due to the mechanical response in $Pr_xCe_{1-x}O_{2-\delta}$ (PCO) (δ is oxygen deficiency) films as a result of applied bias (Swallow *et al.*, 2017). However, the displacements produced were too small for practical use. The ECM-based actuator with a sandwich-like structure was recently fabricated by Makagon et al. (Makagon *et al.*, 2021) It is able to produce micron-size displacements and long-term stability at room temperature. The key innovation behind this actuator that allowed it to operate at room temperature is the use of the active layers (ActLs) made of the metal oxide/20 mol% Gd-doped ceria (20GDC) nanocomposites, serving as working bodies (WBs) (Makagon *et al.*, 2021, Makagon *et al.*, 2022) and separated by a micrometer-thick ionic conductor (IC) made of 20GDC, serving as a solid electrolyte (SE). After applying bias, oxygen ion transport through the IC electrolyte and the WBs undergo changes in volume upon oxidation or reduction, leading to the expansion in one ECM ActL and contraction in the other ECM ActL, inducing μm-sized displacement in the test structure (Makagon *et al.*, 2021).

Ti oxide/20GDC (Makagon *et al.*, 2022, Makagon *et al.*, 2021) (denoted as Ti-GDC for brevity) nanocomposites are found to be integral components functioning as WBs in ECM actuation. The local environment of Ti species was reported to be a distorted TiO_6 octahedron in the case of 38% Ti in the Ti-GDC (Li *et al.*, 2021). In addition, the dimensional changes under the external electric field were shown to be related to the ordering/disordering structural changes of the TiO_6 octahedron (Li *et al.*, 2021). To maximize the ECM response, we hypothesize that the formation of local TiO_x units should play an important role. Predicting the best composition for the ECM effect is difficult because Ti may incorporate in GDC differently, depending on the Ti concentration. Ti can either substitute for Ce atoms in the GDC lattice, form cerium titanates (e.g., $Ce_2Ti_2O_7$, Ce_2TiO_5, $Ce_4Ti_9O_{24}$, $CeTiO_4$, and $CeTi_2O_6$) (Preuss & Gruehn, 1994, Bazuev *et al.*, 1976, Otsuka-Yao-Matsuo *et al.*, 2004, Gionco *et al.*, 2013), or segregate into titania-rich phases. Therefore, studying the concentration-dependent structural changes in the Ti-GDC nanocomposites is essential for understanding and maximizing the mechanical

deformation in the ECM actuator, which until now was designed exclusively by an Edisonian approach.

Although the local structure of Ti-GDC have not been systematically investigated to the best of our knowledge, the CeO_2-TiO_2 system has been studied in the past to some extent because of its promising applications as catalysts (Luo *et al.*, 2015), ferroelectric ceramics (Gao *et al.*, 2015), and electrodes (Kadhim *et al.*, 2021). Watanabe et al. (Watanabe *et al.*, 2009) characterized the crystalline phase and crystallite sizes of nanocrystalline TiO_2-CeO_2 mixed oxides ($Ti_xCe_{1-x}O_2$) by X-ray diffraction (XRD) and found that introducing a small amount of Ce ($x>0.9$) into TiO_2 caused a structural distortion of the anatase phase. In contrast, introducing a small amount of Ti ($x<0.3$) into CeO_2 caused a structural distortion of cubic fluorite phase (Watanabe *et al.*, 2009). However, when the fraction of TiO_2 was in the range between 0.5 and 0.7, their crystalline phase and crystallite sizes were not reported by XRD likely due to the too small sizes of the crystallites and enhanced structural disorder. The formation of $Ce_2Ti_2O_7$, containing ions of eight-fold coordinated Ce and six-fold coordinated Ti, was detected by Raman spectroscopy and optical absorption in CeO_2-TiO_2 with 50 mol% CeO_2 (Gionco *et al.*, 2013). Because the tools for detecting and interpreting structural and compositional details in nanoscale (with dimensions less than ca. 3-5 nm) metal oxides are limited, X-ray absorption spectroscopy (XAS) stands out as the premier technique for this purpose (Rehr & Albers, 2000, Sayers *et al.*, 1971, Farges *et al.*, 1997, Frenkel *et al.*, 2002). X-ray absorption near edge structure (XANES) is particularly sensitive to the local geometry of metal centers, providing information about the oxidation states and local symmetry, and not biased against structural disorder or hampered by nanoscale dimensions of materials (Rehr *et al.*, 1992, Rehr & Albers, 2000, Sayers *et al.*, 1971, Srivastava & Nigam, 1973, Ankudinov *et al.*, 2002). The pre-edge features in the XANES spectra in many cases contain key information about the electronic and structural properties of local environment of metal oxides (Yamamoto, 2008, Srivastava & Nigam, 1973). Taking the Ti K edge pre-edge features in the XANES spectra as an example, as shown by Farges et al. (Farges *et al.*, 1997), the pre-edge energy positions and signal intensities are well separated for fourfold, fivefold, and sixfold coordinated Ti for the Ti^{4+} species, although these results were obtained for standard compounds only. XAS has not been used for a systematic study of CeO_2-TiO_2 mixtures, although results obtained for several compositions of these mixtures were reported (Kityakarn *et al.*, 2013).

The objective of this study is to measure and understand the local structural environment around Ti in Ti-GDC at the broad Ti concentration range. For that, X-ray absorption spectroscopy was employed at both Ti K-edge and Ce L_3-edge. Synchrotron-based X-ray diffraction was used as a complementary method to investigate the long-range structure of Ti-GDC at the same concentrations. To express the series of spectral changes in terms of the number of unique species present in the samples, principal component analysis (PCA) of XANES spectra was used. As a result of the combined XAS, XRD and theoretical XANES modeling, we solved the structures of the Ti-GDC system in each concentration

region and identified the range of concentrations in which the strongest ECM effect is expected.

2. Experiment and data analysis

Nanocomposite thin films were fabricated according to the protocol developed by Makagon et al. (Makagon *et al.*, 2021) In brief, Ti-GDC samples with various Ti concentrations were deposited by a magnetron co-sputtering method on SiO_2 substrates (around 280 μm) with a 100 nm Al adhesion layer. The samples are listed in Table S1 (Supplementary Material) and are denoted as x% Ti-GDC, where x is the concentration of Ti. The deposition conditions are given in Table S1. XRD patterns of Ti-GDC samples were collected at beamline 28-ID (λ = 0.18456 Å), National Synchrotron Light Source II (NSLS-II), Brookhaven National Laboratory. Ti K-edge (4966 eV) X-ray absorption spectra of the Ti-GDC films were measured at the beamline 8-BM of NSLS-II. Ce L_3-edge (5723 eV) X-ray absorption spectra of the Ti-GDC thin films were measured at the beamline 4-3, Stanford Synchrotron Radiation Lightsource (SSRL). All spectra were collected in fluorescence mode. The raw XAFS data were analyzed utilizing the Athena and Artemis interfaces of the Demeter software package (Ravel & Newville, 2005). The spectra were energy-aligned, merged, and edge-step normalized. FEFF software (Rehr *et al.*, 2009, Rehr & Albers, 2000) was utilized to calculate the theoretical XANES spectra based on a specific structural model. Titanium oxide (III), Ti_2O_3, was chosen as a standard to optimize the non-structural parameters.

3. Results and discussion

For the Ti K-edge XANES spectra of all Ti-GDC samples, as shown in Fig. S1, the rising edge positions are close to that of TiO_2, suggesting that the oxidation state of Ti in all Ti-GDC samples is close to Ti^{4+}. The pre-edge feature A corresponds to the *1s* to *3d* transition in Ti and can be used for detecting and quantifying its off-center displacement (Frenkel *et al.*, 2005, Frenkel *et al.*, 2007, Shanthakumar *et al.*, 2006). It appears, based on the calibration method developed by Farges *et al.*, 1997, that, f~~F~~or all samples studied in Ti-GDC films with various Ti concentrations, Ti^{4+} predominantly coordinates with 6 oxygen atoms, as shown in Fig. 1.~~, because the intensities and energy positions of pre-edge peaks for Ti^{4+} species are well separated for the different number of coordinated O atoms around Ti (Farges *et al.*, 1997).~~ This conclusion and the caveats of the Farges' analysis and its applicability for nanoscale, non-bulklike Ti-O compounds, will be discussed below. In addition, for the Ce L_3-edge XANES spectra of all Ti-GDC samples, as shown in Fig. S2, the rising-edge positions are close to that of 20GDC, suggesting that the oxidation states of Ce in all Ti-GDC samples are dominated by Ce^{4+}.

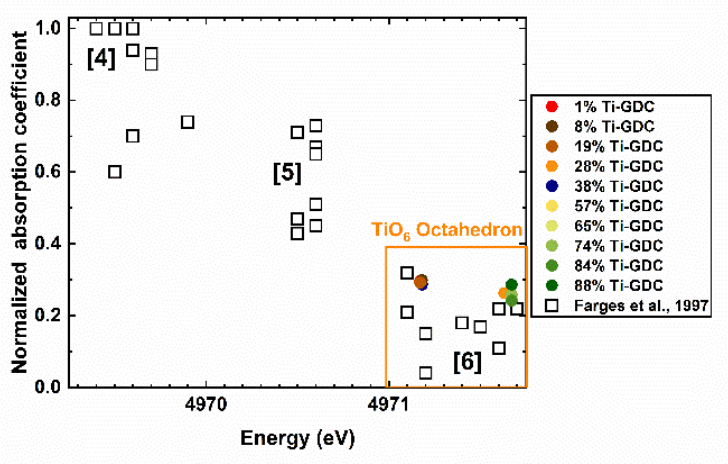

Figure 1 Normalized peak height versus energy position for Ti K-pre-edge features in XANES spectra of TiO_x units in different materials. There are three domains for fourfold, fivefold, and sixfold coordinated Ti (reproduced with permission from Farges et al. (Farges *et al.*, 1997)). Colored symbols correspond to the Ti-GDC samples with different Ti concentrations. 38% Ti-GDC is reproduced from Li et al. (Li *et al.*, 2021) with permission of the International Union of Crystallography.

To group the samples based on the similarity of their spectral features, we employed principal component analysis (PCA). The number of unique species contributing to this series of experimental spectra was obtained (Fay *et al.*, 1992). PCA is a dimensionality reduction technique, which is capable of increasing data interpretability while minimizing information loss (Jolliffe & Cadima, 2016). PCA was applied on Ti K-edge and Ce L_3-edge XANES spectra for all Ti-GDC samples (explained in Section S3 for SI). PCA scree plots for Ti (black) and Ce (red) species are shown in Fig. 2, indicating that the maximum number of distinct species for both Ti and Ce species is three.

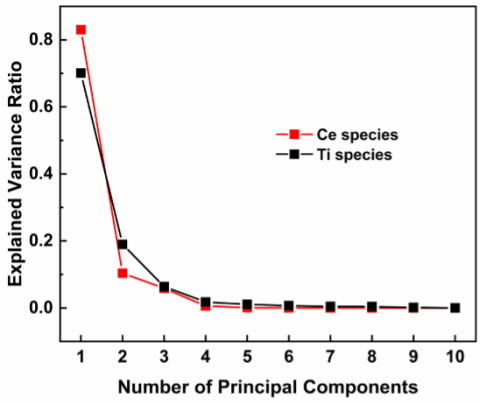

Figure 2 PCA scree plot for Ti species (black) for all Ti-GDC samples and Ce species (red) for all Ti-GDC and 20GDC samples.

The two-dimensional principal subspace (Fig. 3) can be used to group the samples based on the cosine similarity scores (Fig. S3) obtained by analysing Ti K-edge XANES spectra. Cosine similarity scores

are defined as $\cos(\theta) = \frac{\boldsymbol{A}\cdot\boldsymbol{B}}{\|\boldsymbol{A}\|\|\boldsymbol{B}\|}$, where $\boldsymbol{A}$ (or $\boldsymbol{B}$) refer to the vectors from the origin to the point of each sample in the principal subspace. Based on their cosine similarity score, XANES spectra are divided into three groups for Ti species: region I (1%, 8%, and 19% Ti-GDC), transition region (28% Ti-GDC, 38% Ti-GDC reproduced from Li et al. (Li *et al.*, 2021)), and region II (57%, 65%, 74%, 84%, and 88% Ti-GDC). This grouping is consistent with the results obtained by Ce species, as shown in Figs. S4 and S5.

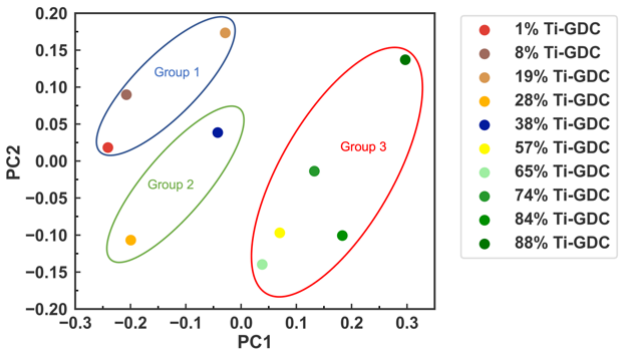

Figure 3 The two-dimensional principal subspace for Ti species. The species are grouped based on the similarity scores shown in Fig. S3.

To gain additional insight into the structural differences between the groups, we examined the XRD data. As shown in Fig. 4, it is apparent that fluorite CeO_2 is found in region I (1%, 8%, and 19% Ti-GDC) and region II (57% Ti-GDC) via a series of (111), (200), (022) and (311) diffraction peaks. However, as shown in Fig. 4, the intensity of the (111) diffraction peak decreased, while the intensity of the (200) and (022) diffraction peaks increased in 57% Ti-GDC, indicating that interaction of Ti oxide with 20GDC distorted the CeO_2 lattice. The rest of the samples do not show any sharp peak features, as shown in Fig. S6, indicating that either ultra-small nanocrystals or amorphous structure would be formed in these Ti-GDC samples. In the following sections, we will describe the local structures of the samples in each region.

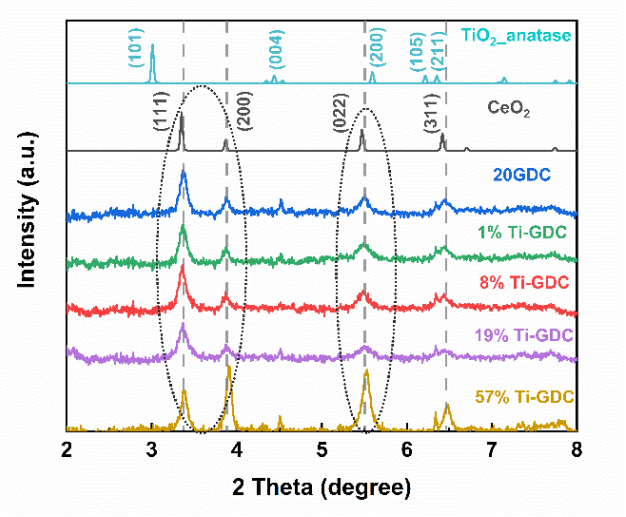

Figure 4 XRD pattern of the 20GDC, 1%, 8%, 19% (region I), and 57% Ti-GDC (region II) with reference fluorite CeO_2 and anatase TiO_2 calculated by VESTA software (Momma & Izumi, 2011).

3.1. Region I

Based on the PCA results, region I contains 1%, 8%, and 19% Ti-GDC samples. Several models can be proposed for the local environments of Ti. One such model (M1) is substitutional, in which Ti replaces the Ce atom in the cubic fluorite structure of CeO_2. The other models correspond to the known Ce-Ti-O stoichiometries with TiO_6 octahedra, namely, M2 ($CeTi_2O_6$), M3 ($Ce_2Ti_2O_7$), M4 (Ce_2TiO_5), and M5 ($CeTiO_3$), as shown in Fig. 5. The key difference in the local structures of Ti and Ce atom environments in these phases is as follows. In M1, Ti is surrounded by 8 oxygen atoms in a cubic TiO_8 unit. Ti is bonded to six oxygen atoms to form corner-sharing TiO_6 octahedra in $CeTi_2O_6$ (M2), and to form corner-sharing TiO_6 octahedra with six equivalent TiO_6 octahedra and edge-sharing with six equivalent CeO_8 in $Ce_2Ti_2O_7$ (M3). In Ce_2TiO_5 (M4), Ce is bonded to six oxygen atoms. In $CeTiO_3$ (M5), Ce is bonded to twelve oxygen atoms to form CeO_{12}, and Ti is coordinated with six oxygen atoms.

We expect that the changes in the local environments between models M1-M5 should be reflected in the corresponding changes in their Ti K-edge XANES spectra. EXAFS data at Ti K-edge (Fig. S7) was theoretically analyzed. The fitting model included the Ti-O scattering path, and its parameters were: the coordination number, correction to the bond length, its variance and the energy origin correction. The amplitude reduction factor was obtained by analysis of bulk anatase EXAFS data and fixed in the fitting of all Ti-GDC samples, which is a standard procedure. The data and fits are shown in Fig. S8. The fitting results are given in Table S2. The Table S2 demonstrates, in agreement with the XANES results already reported in our manuscript, that the coordination number of Ti-O bonds is not consistent with substitutional model (for which Ti-O coordination number should be equal to 8). A precise model of Ti environment is not easy to glean from EXAFS analysis, due to the uncertainty in the amplitude factor obtained by EXAFS (0.6 ± 0.2) and the limited k-range (only the 2-9 $Å^{-1}$ k-range could be used).

~~However, the reduction of Ti–O coordination number with respect to 6 in disordered, nano-sized anatase phases of TiO_2 has been predicted and observed earlier. Thus, to~~In order to identify the possible structures of Ti species, we performed theoretical XANES modeling. The experimental XANES spectrum of Ti_2O_3, as shown in Fig. S9, was chosen as a standard to optimize the modeling (using FEFF code) parameters. The theoretical spectrum of Ti_2O_3 contains two key features (A and B) seen also in the experimental spectrum. Fig. 5 shows that the theoretical spectra of $CeTi_2O_6$ and Ce_2TiO_5 are the best models for reproducing the two key features (A and B) of the experimental data. However, as shown by the Ce L_3-edge spectra (Fig. S2 (b)), the local structure of Ce is similar to that in 20GDC, implying that the Ce ions in all Ti-GDC samples in region I are coordinated with eight oxygen atoms, as opposed to the six oxygen atoms in Ce_2TiO_5. Therefore, the $CeTi_2O_6$ structure, which contains the similar Ce environment as that of 20GDC, wins (our PCA analysis for Ce L_3 edge XANES is inconsistent with the mixed Ce environment in region 1, as shown in Figs. S4 and S5) and we identify it as the prevailing model of the local structure of Ti in region I.

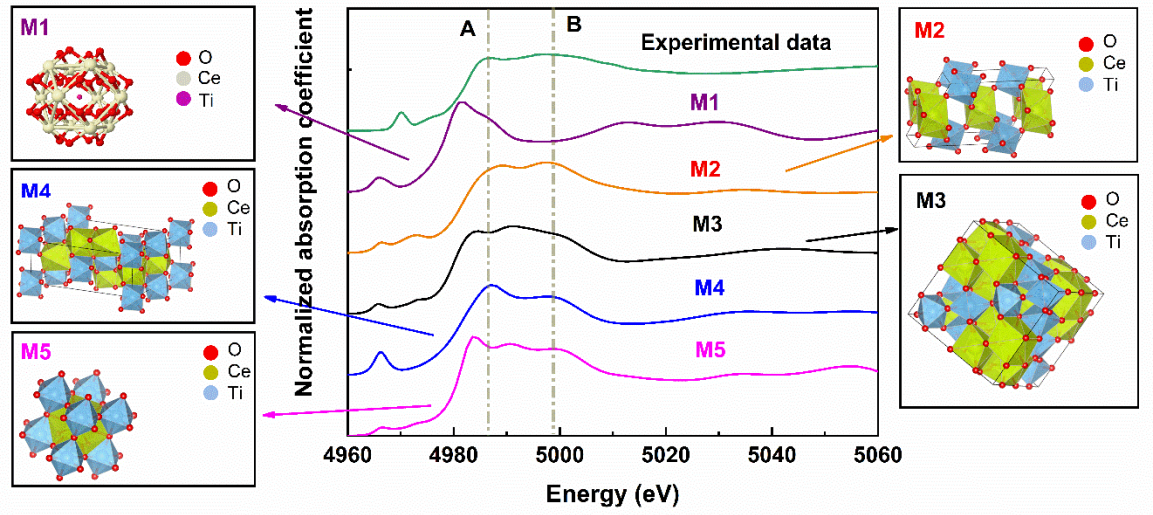

Figure 5 Experimental XANES spectra of Ti atoms in 8% Ti-GDC and simulated XANES spectra of Ti atoms in M1 (Ti replaces Ce in CeO_2), M2 ($CeTi_2O_6$), M3 ($Ce_2Ti_2O_7$), M4 (Ce_2TiO_5), and M5 ($CeTiO_3$). The structure files for M1-M5 are obtained from the Materials Project database (Petousis *et al.*, 2017, Munro *et al.*, 2020, Patel *et al.*, 2019, Jain *et al.*, 2013) and rendered using VESTA (Momma & Izumi, 2011).

3.2. Region II

Region II contains 57%, 65%, 74%, 84%, and 88% Ti-GDC samples. According to Fig. 1, the local environment of Ti is octahedral. In contrast to the pre-edge features in the Ti-GDC samples in region I (Fig. S1), the dominant feature in the pre-edge region is the split into A1 and A2 features, as shown in Fig. 6. The position of the A1, A2, and A3 features are similar to the anatase phase reported by Ke et al. (Ke *et al.*, 2020), but the intensity of these features is much higher for the Ti-GDC samples in our

work. The intensity of the pre-edge features is weak in centrosymmetric environments (Luca *et al.*, 1998), and increases as the environment is distorted. Empirical approaches have been used by Luca et al. (Luca *et al.*, 1998) to establish correlations between the Ti K pre-edge transitions in anatase-TiO_2, indicating that the intensity ratio (I_{A1}/I_{A2}) of the Ti K-pre-edge feature A1 to A2 transitions (equivalent peaks in Luca et al. [41] are labeled as A2 and A3 respectively) increases as particle size decreases, as well as the surface area-to-volume ratio of the particles increases. Farges et al. (Farges *et al.*, 1996) demonstrated that the A1 peak is due to the pentacoordinated Ti atoms. Zhang et al. (Zhang *et al.*, 2008) simulated the amorphous nano-TiO_2 structure by utilizing reverse Monte Carlo (RMC) and demonstrated that feature A1 was also from the distorted Ti-O octahedra. EXAFS analysis of samples in Region II, as shown in Table S2 (SI), indicate that the coordination numbers decrease below 6 at high Ti concentration, although the trend is difficult to identify due to the experimental error bars. A reduction of Ti-O coordination number with respect to the bulk analogue (anatase) of 6 is expected in the case of nano-sized TiO_2, in which the contribution ~~to~~ of the under-coordinated Ti atoms on the surface lowers the average coordination number. This effect was also predicted by simulations (Zhang *et al.*, 2008) and observed in several experimental studies (Shkrob *et al.*, 2004, Rajh *et al.*, 2002, Chen *et al.*, 1999). Thus, we propose that the disordered nanoscale TiO_2 structure was formed in region II.

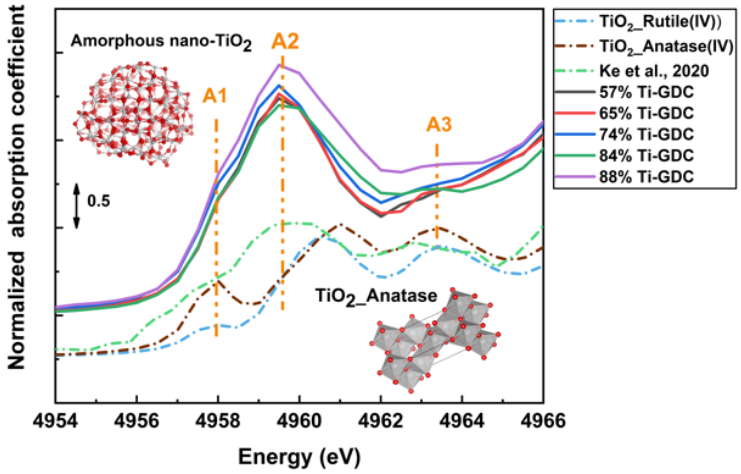

Figure 6 Ti K-pre-edge features for Ti-GDC samples in region II. The distorted anatase Ti K-edge spectrum and reverse Monte Carlo generated amorphous nano-TiO_2 structure are reproduced with permission from Ke et. al. (Ke *et al.*, 2020) and Zhang et. al. (Zhang *et al.*, 2008) respectively. The structure of TiO_2_anatase was generated using information from Materials Project database (Petousis *et al.*, 2017, Munro *et al.*, 2020, Patel *et al.*, 2019, Jain *et al.*, 2013).

As shown in Fig. 7 (top), there are two main Ce L_3-edge peaks: peak A ($2p^6 5d$ state), which is only expected for Ce^{4+} species, and peak B ($2p^5 5d$ * $\underline{L}$ state), which originates from the charge transfer from oxygen to the Ce 4f orbital (Soldatov *et al.*, 1994, Kossoy *et al.*, 2013, Bianconi *et al.*, 1987). $2\underline{p}$ denotes the empty state in the $2p$ shell and $\underline{L}$ denotes an empty state in the neighboring oxygen orbital. Following

the process described by Overbury et al. (Overbury *et al.*, 1998), the 20GDC data was subtracted from each of the Ti-GDC data, and the differences between the Ti-GDC and GDC data were shown in Fig. 7 (bottom). With the increasing Ti concentration, there is progressive decrease in the intensity of peaks B at 5731 eV, but at the same time, peak B' is growing, corresponding to the reduction of Ce species. Hence, both Ce^{4+} and Ce^{3+} species are present in the Ti-GDC samples in region II.

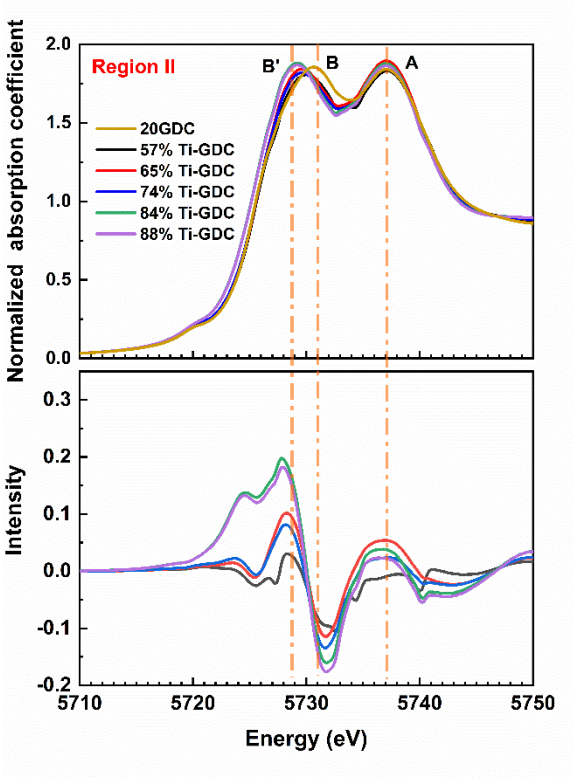

Figure 7 Ce L_3-edge XANES spectra are shown in the top pane for the 57%, 65%, 74%, 84%, 88% Ti-GDC sample, and 20 GDC sample. 20GDC data has been subtracted from each spectrum. The difference between the Ti-GDC and 20GDC data is shown in the bottom pane.

3.3. Transition region

According to the results obtained by PCA, 28% Ti-GDC sample is not identified as either region I or region II. According to Fig. 1, the local environment of Ti is octahedral. As shown in Fig. 8(a), the normalized Ti K-pre-edge XANES spectrum of 28% Ti-GDC is close to that in the 19% Ti-GDC sample, with only one prominent peak rather than the two splitting peaks in 57% Ti-GDC samples. In addition, the intensity of the pre-edge peak A in 28% Ti-GDC is lower than that in the 19% Ti-GDC sample. Moreover, as shown in Fig. 8 (b), the position of the peak B of the Ce L_3-edge XANES spectrum of 28% Ti-GDC is between 20GDC and 57% Ti-GDC sample, indicating the coexistence of the Ce^{4+} and Ce^{3+} species. Therefore, the region between region I and region II is transitional between nanoscale cerium titanate structure and phase - segregated disordered titania.

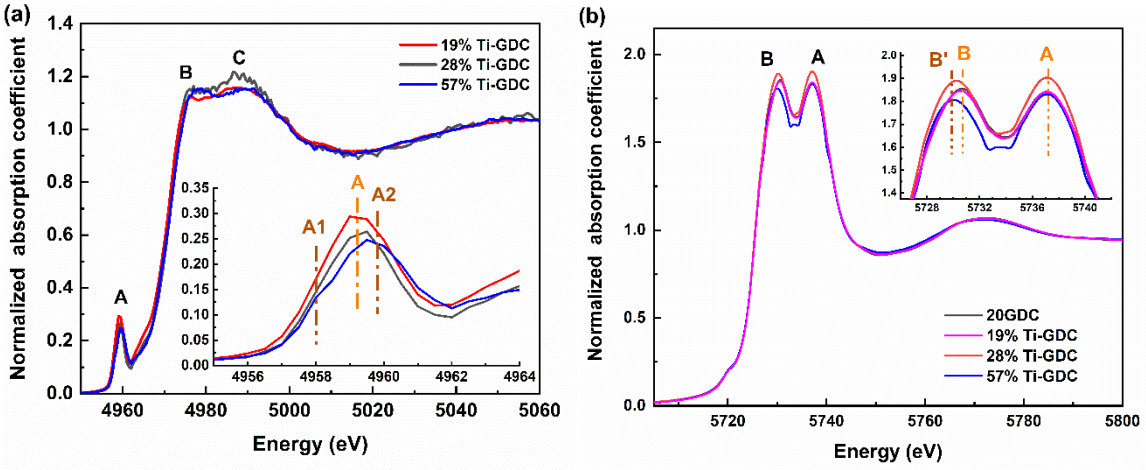

Figure 8 (a) Normalized Ti K-edge XANES spectra of 28% Ti-GDC and the reference: 19% Ti-GDC and 57% Ti-GDC. Inset: the enlarged pre-edge region. (b) Normalized Ce L_3-edge XANES spectra of 28% Ti-GDC and the references: 20GDC, 19% Ti-GDC, and 57% Ti-GDC. Inset: the enlarged region of the main peaks.

Based on the combination of experimental and theoretical XANES spectroscopy of Ti K and Ce L_3 edges and XRD studies, we identified the range of Ti concentrations (from 28% to 88%, using multiple Ti-GDC samples with controlled Ti compositions) in which TiO_x can be detected as a separate region. This result is consistent with the previous work in which 38% Ti in Ti-GDC was found to be electro-chemo-mechanically active (Makagon *et al.*, 2021). TiO_x with locally disordered octahedral TiO_6 units undergo rapid oxidation and reduction in the ECM effect. However, ECM devices with working body consisting of 100% TiO_x show immediate saturation of ECM response due to lack of oxygen transport (Mishuk *et al.*, 2019). Hence, the coexistence of the Ce^{4+} and Ce^{3+} species should be the key descriptor for characterizing oxygen diffusion in the ECM actuators. Based on this study we propose that other mixed TiO_2-CeO_2 systems within the broader range of Ti concentrations can also be ECM-active. For a search of the strongest effect in Ti-GDC composites we propose to investigate the concentrations in the transition region (between 19 and 57 mol % Ti) due to the observed strong local distortion of Ti in the TiO_6 units (hence, capable to generate large local strains) and coexistence of Ce^{4+} and Ce^{3+} (hence, facilitating oxygen transport). Our analysis methodology developed for this material can be used for analysing a large class of functional mixed metal oxides.

4. Conclusions

The volumetric changes in the two working bodies made by TiO_x/20GDC (Ti-GDC) are essential to generate large mechanical deformation in the ECM actuator. Both XAS and XRD were applied to study the structural changes of the Ti-GDC and clarify the local structure of Ti and Ce in Ti-GDC with various Ti concentrations. We detected three different types of local structural units at different Ti concentrations using principal component analysis of XANES spectra and identified the likely

structures each region. In regions I and II, the local structure of Ce species is similar to that in fluorite CeO_2. Nanoscale cerium titanates were formed in region I, while in region II, the disordered nano-TiO_2 structure was found. Meanwhile, both Ce^{4+} and Ce^{3+} species are present in the Ti-GDC samples in region II. Between regions I and II, there is a transition region containing TiO_x units with strongly distorted TiO_6 octahedra along with coexisting Ce^{4+} and Ce^{3+} species. Our results will be helpful for future studies that will aim to link the ECM and other electromechanical effects (e.g., electrostriction) to the local geometric and electronic properties of mixed oxides.

Acknowledgements This research used beamlines 8-BM and 28-ID-2 of the National Synchrotron Light Source II (NSLS-II), a U.S. DOE Office of Science User Facility operated for the DOE Office of Science by Brookhaven National Laboratory under contract no. DE-SC0012704. Use of the Stanford Synchrotron Radiation Lightsource, SLAC National Accelerator Laboratory, is supported by the U.S. Department of Energy, Office of Science, Office of Basic Energy Sciences under Contract No. DE-AC02-76SF00515. We gratefully acknowledge Dr. Yonghua Du for his support of these experiments at the 8-BM beamline, Dr. Sanjit Ghose - for his support of these experiments at the 28-ID-2 beamline of NSLS-II and Dr. Erik Nelson for his support at the 4-3 beamline of SSRL. We acknowledge support by the Synchrotron Catalysis Consortium funded by the US Department of Energy, Office of Science, Office of Basic Energy Sciences, Grant No. DE-SC0012335. AIF acknowledges support by Weston Visiting Professorship during his stay at the Weizmann Institute of Science.

References

Ankudinov, A., Rehr, J., Low, J. J. & Bare, S. R. (2002). *The Journal of chemical physics* **116**, 1911-1919.

Bazuev, G., Makarova, O., Zhilyaev, V. & Shveikin, G. (1976). *Russ. J. Inorg Chem* **21**,

Bianconi, A., Marcelli, A., Dexpert, H., Karnatak, R., Kotani, A., Jo, T. & Petiau, J. (1987). *Physical Review B* **35**, 806.

Bishop, S., Marrocchelli, D., Chatzichristodoulou, C., Perry, N. H., Mogensen, M. B., Tuller, H. & Wachsman, E. (2014). *Annual Review of Materials Research* **44**, 205-239.

Bishop, S. R., Perry, N. H., Marrocchelli, D., Sheldon, B. W., Zuev, A. Y., Tsvetkov, D. S., Santiso, J., Moreno, R., Hull, S. & Nicholas, J. D. (2017). *Electro-chemo-mechanics of solids*. Springer.

Chen, L. X., Rajh, T., Jäger, W., Nedeljkovic, J. & Thurnauer, M. C. (1999). *Journal of synchrotron radiation* **6**, 445-447.

Farges, F., Brown, G. E. & Rehr, J. (1997). *Physical Review B* **56**, 1809.

Farges, F., Brown Jr, G. E. & Rehr, J. J. (1996). *Geochimica et Cosmochimica acta* **60**, 3023-3038.

Fay, M. J., Proctor, A., Hoffmann, D. P., Houalla, M. & Hercules, D. M. (1992). *Microchimica Acta* **109**, 281-293.

Frenkel, A. I., Ehre, D., Lyahovitskaya, V., Kanner, L., Wachtel, E. & Lubomirsky, I. (2007). *Physical Review Letters* **99**, 215502.

Frenkel, A. I., Feldman, Y., Lyahovitskaya, V., Wachtel, E. & Lubomirsky, I. (2005). *Physical Review B* **71**, 024116.

Frenkel, A. I., Kleifeld, O., Wasserman, S. R. & Sagi, I. (2002). *The Journal of chemical physics* **116**, 9449-9456.

Gao, Z., Liu, L., Han, X., Meng, X., Cao, L., Ma, G., Liu, Y., Yang, J., Xie, Q. & He, H. (2015). *Journal of the American Ceramic Society* **98**, 3930-3934.
Gionco, C., Paganini, M. C., Agnoli, S., Reeder, A. E. & Giamello, E. (2013). *Journal of Materials Chemistry A* **1**, 10918-10926.
Jain, A., Ong, S. P., Hautier, G., Chen, W., Richards, W. D., Dacek, S., Cholia, S., Gunter, D., Skinner, D., Ceder, G. & Persson, K. A. (2013). *APL Materials* **1**, 011002.
Jolliffe, I. T. & Cadima, J. (2016). *Philosophical Transactions of the Royal Society A: Mathematical, Physical and Engineering Sciences* **374**, 20150202.
Kadhim, F. M., Baqer, A. A., Shanan, Z. J. & Tameem, M. K. (2021). *AIP Conference Proceedings*, p. 180009. AIP Publishing LLC.
Ke, W., Liu, Y., Wang, X., Qin, X., Chen, L., Palomino, R. M., Simonovis, J. P., Lee, I., Waluyo, I. & Rodriguez, J. A. (2020). *Nano Letters* **20**, 6884-6890.
Kityakarn, S., Worayingyong, A., Suramitr, A. & Smith, M. (2013). *Materials Chemistry and Physics* **139**, 543-549.
Kossoy, A., Wang, Q., Korobko, R., Grover, V., Feldman, Y., Wachtel, E., Tyagi, A., Frenkel, A. & Lubomirsky, I. (2013). *Physical Review B* **87**, 054101.
Li, J., Li, Y., Routh, P. K., Makagon, E., Lubomirsky, I. & Frenkel, A. I. (2021). *Journal of Synchrotron Radiation* **28**,
Luca, V., Djajanti, S. & Howe, R. F. (1998). *The Journal of Physical Chemistry B* **102**, 10650-10657.
Luo, S., Nguyen-Phan, T.-D., Johnston-Peck, A. C., Barrio, L., Sallis, S., Arena, D. A., Kundu, S., Xu, W., Piper, L. F. & Stach, E. A. (2015). *The Journal of Physical Chemistry C* **119**, 2669-2679.
Makagon, E., Li, J., Li, Y., Wachtel, E., Frenkel, A. I. & Lubomirsky, I. (2022). *Solid state ionics* **379**, 115913.
Makagon, E., Wachtel, E., Houben, L., Cohen, S. R., Li, Y., Li, J., Frenkel, A. I. & Lubomirsky, I. (2021). *Advanced functional materials* **31**, 2006712.
Mishuk, E., Ushakov, A., Makagon, E., Cohen, S. R., Wachtel, E., Paul, T., Tsur, Y., Shur, V. Y., Kholkin, A. & Lubomirsky, I. (2019). *Advanced Materials Interfaces* **6**, 1801592.
Momma, K. & Izumi, F. (2011). *Journal of applied crystallography* **44**, 1272-1276.
Munro, J. M., Latimer, K., Horton, M. K., Dwaraknath, S. & Persson, K. A. (2020). *npj Computational Materials* **6**, 1-6.
Otsuka-Yao-Matsuo, S., Omata, T. & Yoshimura, M. (2004). *Journal of alloys and compounds* **376**, 262-267.
Overbury, S., Huntley, D., Mullins, D. & Glavee, G. (1998). *Catalysis letters* **51**, 133-138.
Patel, A. M., Nørskov, J. K., Persson, K. A. & Montoya, J. H. (2019). *Physical Chemistry Chemical Physics* **21**, 25323-25327.
Petousis, I., Mrdjenovich, D., Ballouz, E., Liu, M., Winston, D., Chen, W., Graf, T., Schladt, T. D., Persson, K. A. & Prinz, F. B. (2017). *Scientific data* **4**, 1-12.
Preuss, A. & Gruehn, R. (1994). *Journal of Solid State Chemistry* **110**, 363-369.
Rajh, T., Chen, L., Lukas, K., Liu, T., Thurnauer, M. & Tiede, D. (2002). *The Journal of Physical Chemistry B* **106**, 10543-10552.
Ravel, B. & Newville, M. (2005). *Journal of synchrotron radiation* **12**, 537-541.
Rehr, J. J. & Albers, R. C. (2000). *Reviews of modern physics* **72**, 621.
Rehr, J. J., Albers, R. C. & Zabinsky, S. I. (1992). *Phys Rev Lett* **69**, 3397-3400.
Rehr, J. J., Kas, J. J., Prange, M. P., Sorini, A. P., Takimoto, Y. & Vila, F. (2009). *Comptes Rendus Physique* **10**, 548-559.
Sayers, D. E., Stern, E. A. & Lytle, F. W. (1971). *Physical review letters* **27**, 1204.
Sethuraman, V. A., Chon, M. J., Shimshak, M., Srinivasan, V. & Guduru, P. R. (2010). *Journal of Power Sources* **195**, 5062-5066.
Shanthakumar, P., Balasubramanian, M., Pease, D. M., Frenkel, A. I., Potrepka, D. M., Kraizman, V., Budnick, J. I. & Hines, W. A. (2006). *Physical Review B* **74**, 174103.
Shkrob, I. A., Sauer, M. C. & Gosztola, D. (2004). *The Journal of Physical Chemistry B* **108**, 12512-12517.
Soldatov, A., Ivanchenko, T., Della Longa, S., Kotani, A., Iwamoto, Y. & Bianconi, A. (1994). *Physical Review B* **50**, 5074.

Srivastava, U. & Nigam, H. (1973). *Coordination Chemistry Reviews* **9**, 275-310.
Swallow, J., Woodford, W., Chen, Y., Lu, Q., Kim, J., Chen, D., Chiang, Y.-M., Carter, W., Yildiz, B. & Tuller, H. (2014). *Journal of Electroceramics* **32**, 3-27.
Swallow, J. G., Kim, J. J., Maloney, J. M., Chen, D., Smith, J. F., Bishop, S. R., Tuller, H. L. & Van Vliet, K. J. (2017). *Nature materials* **16**, 749-754.
Tuller, H. L. & Bishop, S. R. (2011). *Annual Review of Materials Research* **41**, 369-398.
Wang, X., Fan, F., Wang, J., Wang, H., Tao, S., Yang, A., Liu, Y., Beng Chew, H., Mao, S. X. & Zhu, T. (2015). *Nature communications* **6**, 1-7.
Watanabe, S., Ma, X. & Song, C. (2009). *The Journal of Physical Chemistry C* **113**, 14249-14257.
Yamamoto, T. (2008). *X-Ray Spectrometry: An International Journal* **37**, 572-584.
Zhang, H., Chen, B., Banfield, J. F. & Waychunas, G. A. (2008). *Physical Review B* **78**, 214106.

Supporting information

S1. Sample details

Table S1 Deposition conditions for Ti-GDC nanocomposites deposited on SiO_2 substrates with Al stress relief layer. All samples were deposited at room temperature.

Sample	Ti/(Ti+Gd+Ce) (at%)	GDC Power (W)	Ti Power (W)	O_2 flow (sccm)	$O_2/(O_2+Ar)$ (%)	Deposition time (hr)
20GDC	0	110	0	3	9	3
1% Ti-GDC	1	110	70	3	9	3
8% Ti-GDC	8	110	170	3	9	3
19% Ti-GDC	19	110	230	3	9	3
28% Ti-GDC	28	50	150	3	9	3
38% Ti-GDC	38	100	150	3	8	3
57% Ti-GDC	57	85	137	1.5	5	3
65% Ti-GDC	65	85	150	1.5	5	3
74% Ti-GDC	74	85	175	1.5	5	4
84% Ti-GDC	84	65	200	1.5	5	3
88% Ti-GDC	88	65	200	1.5	5	6

S2. Ti K-edge and Ce L_3-edge XANES of TiO_x-20GDC nanocomposites

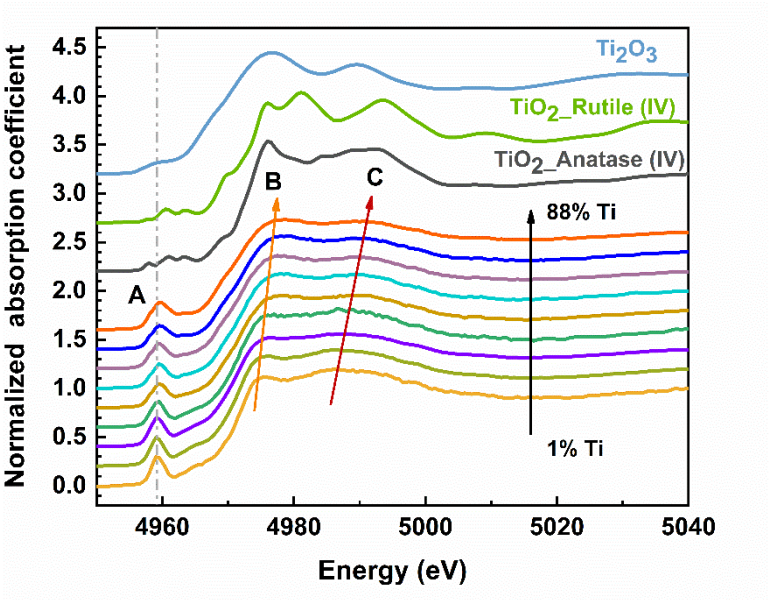

Figure S1 Normalized Ti K-edge XANES spectra of all samples with titanium oxides standards: Ti_2O_3 and TiO_2 (rutile and anatase). Spectra are vertically stacked for comparison.

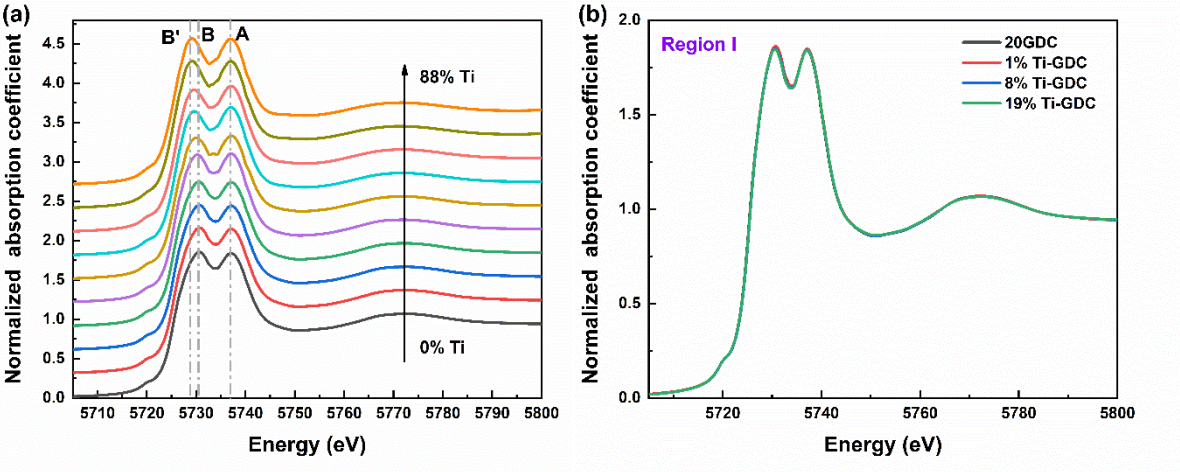

Figure S2 (a) Normalized Ce L_3-edge XANES spectra (stacked) of all samples, (b) samples in Region I only (overlayed).

S3. Dimensionality reduction and clustering of XANES using Principal Component Analysis (PCA)

XANES spectra in the energy range of E_0 - 20eV to E_0 + 80eV with E_0= 4971.23eV were selected for spectral similarity in the reduced principal space. PCA was applied to reduce the dimensionality of each XANES spectra in (energy axis) and analyze the similarity of reduced XANES spectra based on cosine similarity of vectors in principal directions. For 10 different XANES spectra, 10 eigenvalues were obtained. As shown in Fig. 2, the variance in the sample is captured by first 3 principal components, indicating the presence of 3 potential clusters. Scatterplot of first two principal components (Fig. 3) shows a visual representation of each cluster with each XANES spectra represented by only first 2 principal components. For a more objective clustering, vectors consisting of 10 principal components for each sample were used to obtained cosine similarity as defined in the main text. Figure S3, shows the cosine similarity values and nearest neighbor clusters according to these values. Similar study was carried out on Ce-L_3-edge XANES spectra as well and the results are shown in Figure S4 and Figure S5.

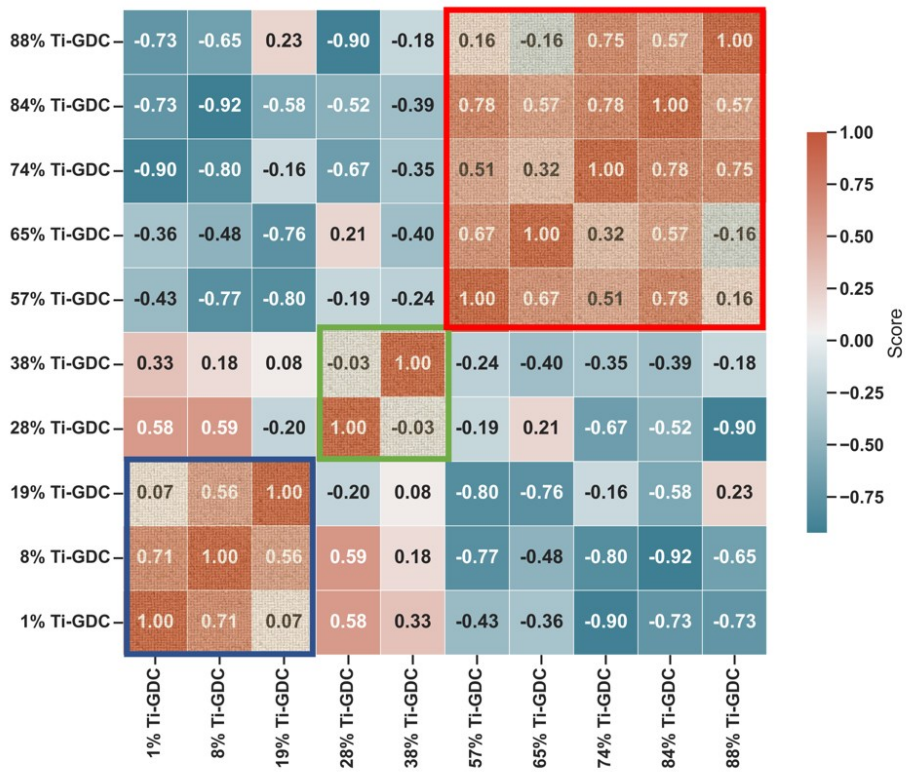

Figure S3 Heatmap for Ti species generated using the cosine similarity in principal subspace. The samples are grouped based on nearest neighbour in the similarity score.

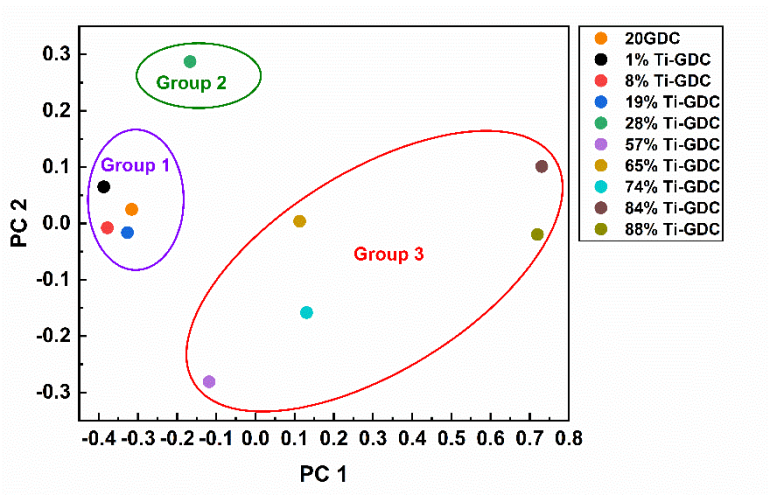

Figure S4 The two-dimensional principal subspace for Ce species. The species are grouped based on the similarity scores shown in Fig. S5.

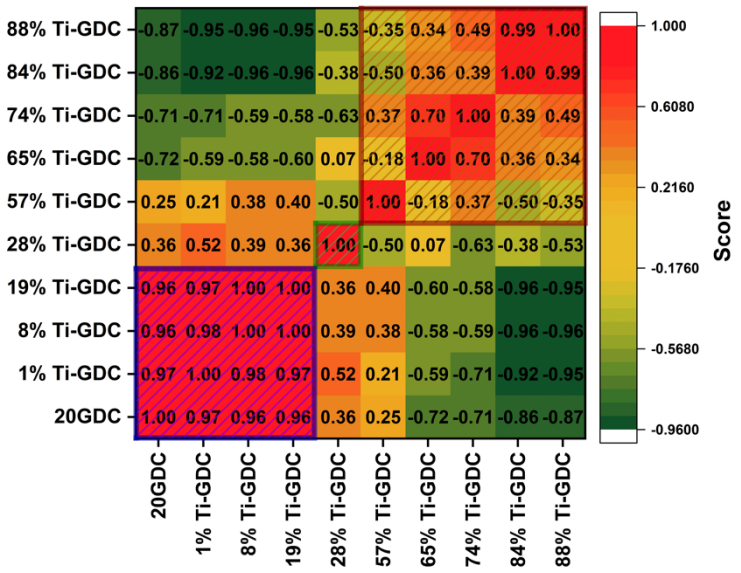

Figure S5 Heatmap for Ce species generated using the cosine similarity in principal subspace. The samples are grouped based on nearest neighbour in the similarity score.

S4. X-ray diffraction spectra of Ti-GDC

Figure 4 shows the XRD spectra for low %Ti-GDC and showing Bragg peaks corresponding to 20GDC. Remaining XRD spectra are shown below in Figure S6.

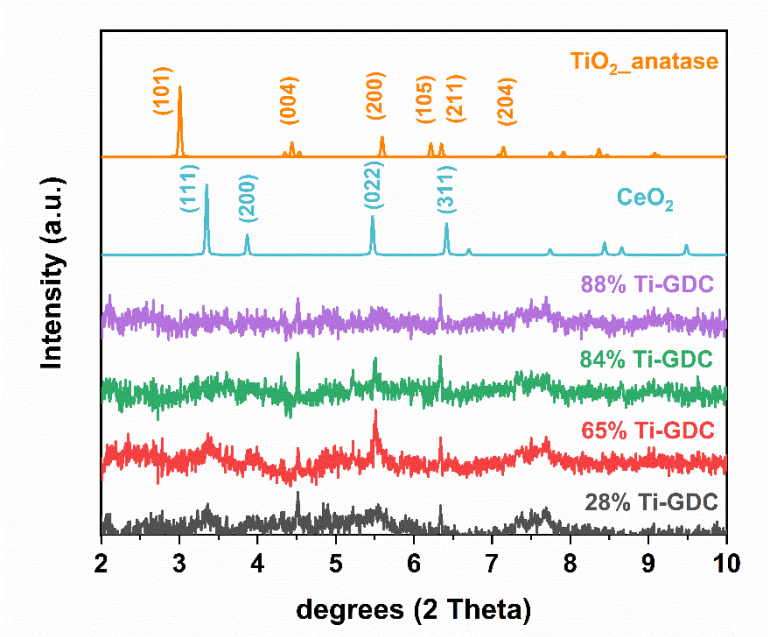

Figure S6 XRD pattern of the 28% Ti-GDC, 65% Ti-GDC, 84% Ti-GDC, and 88% Ti-GDC with CeO_2 and TiO_2 (anatase) standards.

S5. Ti K-edge EXAFS analysis of TiO_x-20GDC nanocomposites

Figure S7 shows the EXAFS spectra in k-space and r-space along with a sample consisting of TiO_2-Anatase. Figure S8 shows the data and theoretical fits in r-space for all samples analysed at Ti K-edge. Table S2 contains the best fit results.

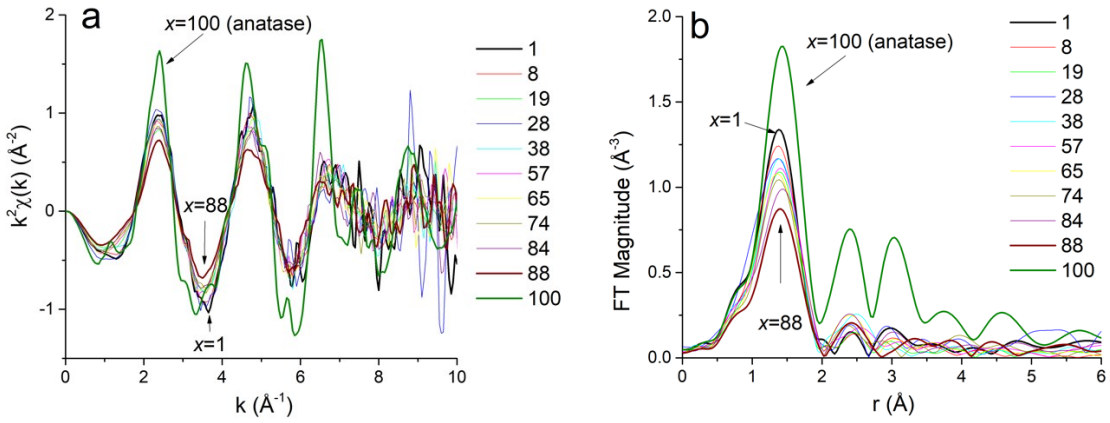

Figure S7 XANES data (a), k^2-weighted Ti K-edge EXAFS data in k-space, and (b) Fourier transform magnitudes of the k^2-weighted EXAFS data TiO_2 (anatase) and Ti-GDC samples.

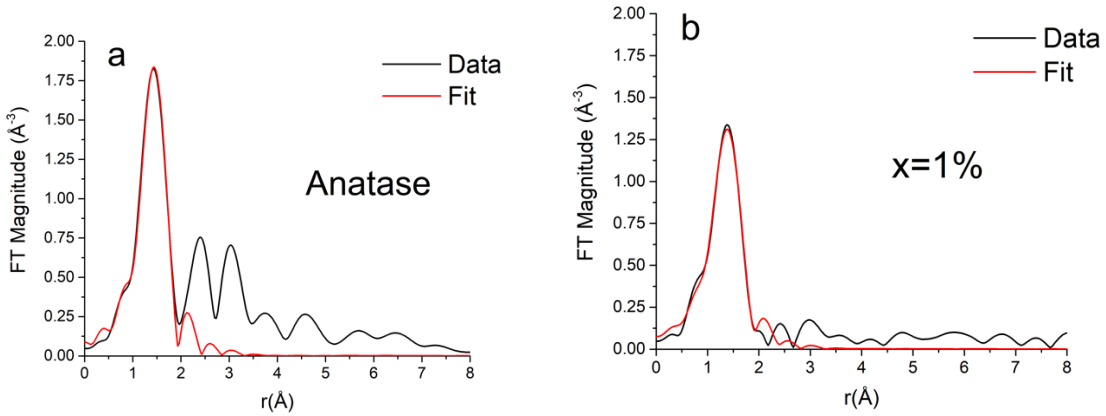

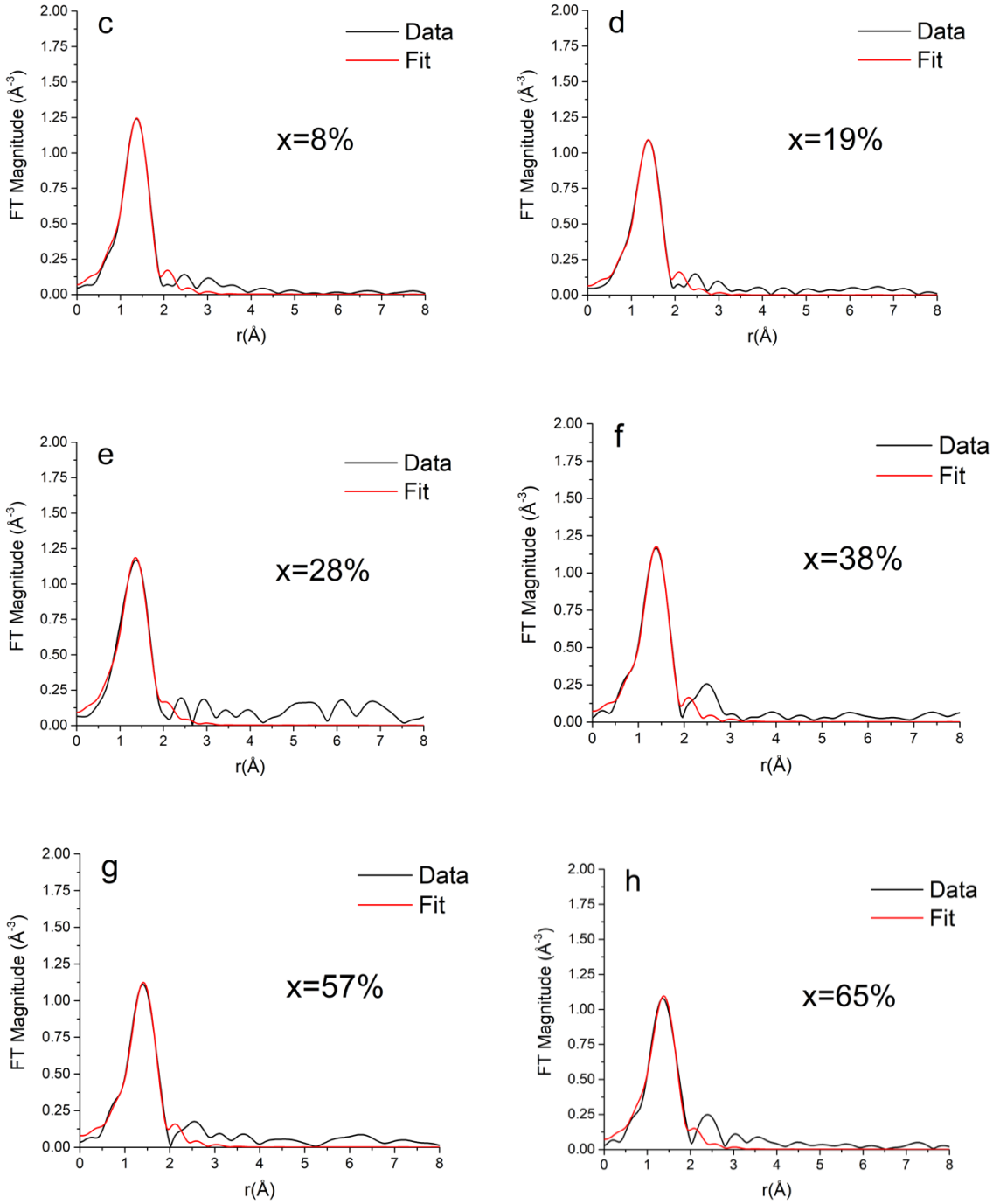
c
Data
Fit
x=8%
d
x=19%
e
x=28%
f
x=38%
g
x=57%
h
x=65%
FT Magnitude (Å-3)
r(Å)

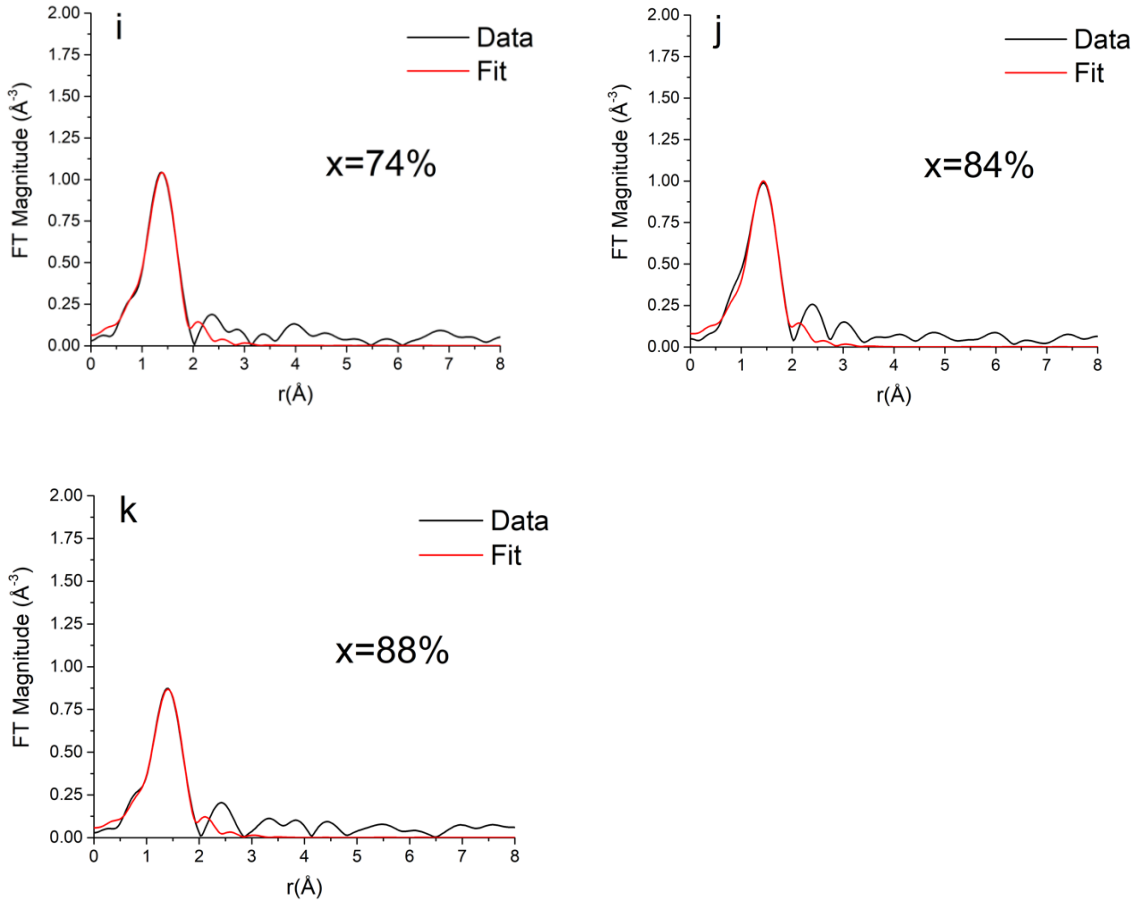

Figure S8 Fourier transform magnitudes of k^2-weighted EXAFS data and theoretical fits for the TiO_2 – anatase (a) and Ti-GDC samples (b-k).

Table S2 Fit results for the Ti-GDC samples and TiO_2 – anatase (x=100). The S_0^2 parameter (the passive electron reduction factor) was determined from the fit to the anatase structure to be equal to 0.6 ± 0.2 and fixed to 0.6 in the fits for the rest of the samples.

x	N_{Ti-O}	R_{Ti-O} (Å)	σ^2_{Ti-O} (Å^2)
1	5.3(7)	1.91(1)	0.006(2)
8	5.6(9)	1.91(2)	0.007(3)
19	4.5(8)	1.92(2)	0.006(3)
28	6.8(1.4)	1.91(2)	0.012(4)
38	4.8(1.3)	1.92(3)	0.006(4)
57	5.0(1.1)	1.94(2)	0.007(4)

65	5.6(2.1)	1.92(4)	0.010(6)
74	4.6(1.1)	1.92(2)	0.007(4)
84	4.5(1.2)	1.95(3)	0.008(5)
88	3.7(6)	1.92(3)	0.007(3)
100 (anatase)	6 (fixed)	1.95(3)	0.002(5)

S6. FEFF parameter optimization for XANES modelling

Ti_2O_3 structure and corresponding experimental and FEFF generated theoretical spectra (shown in Fig S9) were used to validate the non-structural FEFF parameters which are further used to simulate the spectra of other Ti species.

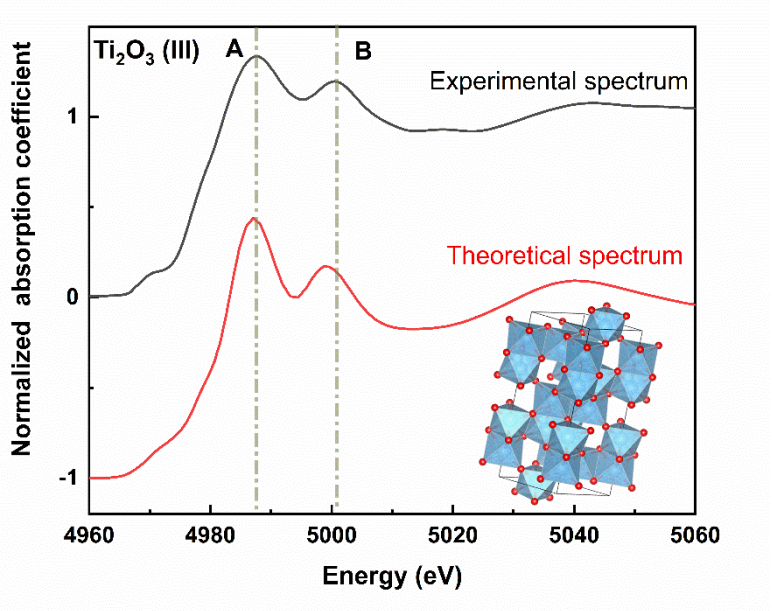

Figure S9 Experimental and simulated XANES spectra of Ti atoms in Ti_2O_3.